Atomic Layer Deposition of Hierarchical CNTs@$FePO_4$ Architecture as a 3D Electrode for Lithium-Ion and Sodium-Ion Batteries

*Jian Liu, Biqiong Wang, Qian Sun, Ruying Li, Tsun-Kong Sham, and Xueliang Sun**

3D microbatteries hold great promise as on-board energy supply systems for microelectronic devices. The construction of 3D microbatteries relies on the development of film deposition techniques that can enable coatings of uniform electrode and electrolyte materials in high-aspect-ratio substrates. Here, a 3D $FePO_4$ on carbon nanotubes (CNTs@$FePO_4$) structure is fabricated by coating $FePO_4$ on CNTs/carbon paper substrate using atomic layer deposition. Compared to $FePO_4$ on a planar substrate, the 3D CNTs@$FePO_4$ electrode exhibits significantly increased areal capacity and excellent rate capability for lithium-ion and sodium-ion storage. The 3D CNTs@$FePO_4$ maintains areal capacities of 64 and 33 μAh cm^{-2} after 180 cycles for lithium-ion batteries (LIBs) and sodium-ion batteries, which are 16 and 33 times higher than those of planar $FePO_4$ electrode, respectively. Moreover, hybrid 3D CNTs@$FePO_4$@Li_3PO_4 structure is fabricated by coating Li_3PO_4 solid-state electrolyte on 3D CNTs@$FePO_4$. The CNTs@$FePO_4$@Li_3PO_4 electrode shows stable cycling performance in LIBs. Hard X-ray photoemission spectroscopy analysis demonstrates that the Li_3PO_4 coating prevents the formation of undesirable LiF in the solid-electrolyte interphase layer, which is believed to be responsible for the performance degradation in CNTs@$FePO_4$. This work paves the way to building reliable 3D nanostructured electrode and electrolyte architectures for high areal capacity microbatteries.

1. Introduction

The continuous downsizing of microelectronic devices requires on-board energy storage systems with comparable dimensions. All-solid-state microbatteries with 3D architectures have been seen as a viable solution to this urgent demand. In comparison to conventional 2D planar thin-film batteries, 3D structured microbatteries can provide higher areal energy capacities (μAh cm^{-2}) due to the increased specific surface area of active materials in the same footprint, while still deliver good power densities as a result of short Li^+ diffusion paths.[1,2] In order to realize 3D microbatteries, there is a great need for thin film deposition techniques that can precisely produce thin film electrode and electrolyte materials on high-aspect-ratio substrates. Recently, atomic layer deposition (ALD) appears as a powerful technique for depositing uniform and conformal thin films on such high-aspect-ratio substrates.[3] ALD is based on sequential exposure of gaseous precursors on the target substrates where saturated surface reactions allow deposition of high-quality thin films in a layer-by-layer manner, and the film thickness is controlled in submonolayer accuracy.[4,5] These advantages of ALD promise it great potential for the fabrication of 3D all-solid-state microbatteries. To achieve this ultimate goal, it is essential to develop ALD processes specifically for battery active materials, including the anode, cathode, and solid-state electrolyte.

During the past few years, great progresses have been made to produce these electrochemically active materials by ALD for lithium-ion battery (LIB) applications.[6–9] On one hand, the anode materials that can be synthesized by ALD have been extended from metal oxides (such as TiO_2, SnO_2) to metal sulfides (such as GaS_x).[9,10] Meanwhile, several glass-type solid-state electrolytes, i.e., $LiTaO_3$,[11] Li_3PO_4,[12,13] $Li_xAl_ySi_zO$,[14] and LiPON,[15,16] have been deposited via ALD by using a sub-cycle strategy, and exhibited ionic conductivities of ≈10^{-9}–10^{-7} S cm^{-1} at room temperature (RT). Lithium-containing cathode materials ($LiCoO_2$, $LiMnO_2$, and $LiFePO_4$)[17–19] have also been synthesized using ALD, by carefully designing the surface chemistry employed. More recently, an organic lithium anode, Li-terephthalate, has also been successfully made by using Li(thd) and terephthalic acid as precursors and pairing ALD with molecular layer deposition.[20] With these ALD-deposited electrode materials in place, the next key step toward 3D microbatteries would be the integration of these active materials onto 3D structures to build 3D microelectrodes, which is yet to be demonstrated. Besides LIBs, sodium-ion batteries (SIBs) are recently attracting increasing attention as a low-cost energy storage system.[21–23] Similarly, development of 3D electrode

Dr. J. Liu, B. Wang, Dr. Q. Sun, R. Li, Prof. X. Sun
Department of Mechanical and Materials Engineering
University of Western Ontario
London, ON N6A 5B9, Canada
E-mail: xsun9@uwo.ca
Prof. T.-K. Sham
Department of Chemistry
University of Western Ontario
London, ON N6A 5B7, Canada

DOI: 10.1002/admi.201600468

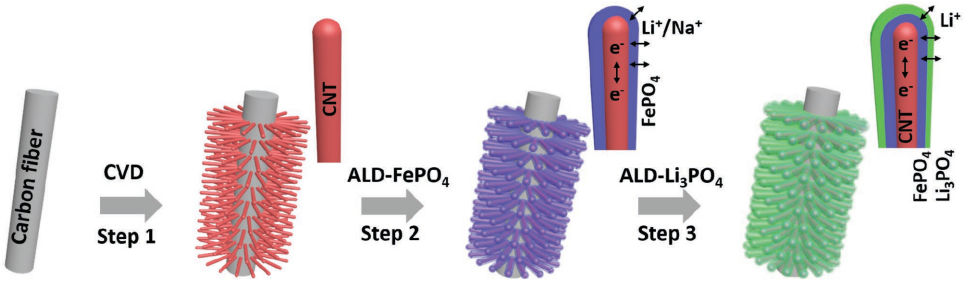

Scheme 1. Schematic diagram of the fabrication process for 3D CNTs@$FePO_4$ and CNTs@$FePO_4$@Li_3PO_4 electrodes. Step 1: Growth of CNTs on carbon papers by a CVD method; Step 2: deposition of amorphous $FePO_4$ on CNTs by ALD; Step 3: coating of Li_3PO_4 solid-state electrolyte on CNTs@$FePO_4$ by ALD.

structure can be an effective approach to achieve high-power SIBs.

Herein, we report the fabrication of a 3D CNT@$FePO_4$ architecture by ALD, using carbon nanotubes (CNTs) grown on carbon papers as 3D conductive substrates, and $FePO_4$ as a cathode material. The 3D CNT@$FePO_4$ structures exhibited much higher areal capacity than $FePO_4$ on a planar substrate for LIBs. Moreover, Li_3PO_4 solid-state electrolyte coating was further applied on the 3D CNT@$FePO_4$ architecture. This engineered CNT@$FePO_4$@Li_3PO_4 microstructure was shown to be electrochemically active in LIBs. Additionally, the as-synthesized 3D CNT@$FePO_4$ structure exhibited good electrochemical activity for sodium-ion storage.

2. Results and Discussion

The fabrication process for 3D CNTs@$FePO_4$ and CNTs@$FePO_4$@Li_3PO_4 electrodes is schematically shown in **Scheme 1**. In the first step, nitrogen-doped CNTs were grown on carbon papers by pyrolyzing melamine at 800 °C in a chemical vapor deposition (CVD) system.[24] In the second step, amorphous $FePO_4$ was deposited on the 3D CNT substrates by ALD, and the thickness of $FePO_4$ layer was controlled by using different ALD cycles (200 and 400 cycles). The samples obtained in the second step are designated as 200-cycle and 400-cycle CNTs@$FePO_4$ respectively hereafter. The CNTs@$FePO_4$ were evaluated as 3D electrodes in LIBs and SIBs, and compared to $FePO_4$ deposited on 2D stainless steel (SS@$FePO_4$) electrode. In the third step, amorphous Li_3PO_4 was subsequently coated on the CNTs@$FePO_4$ samples by ALD, and served as a solid-state electrolyte for LIBs.

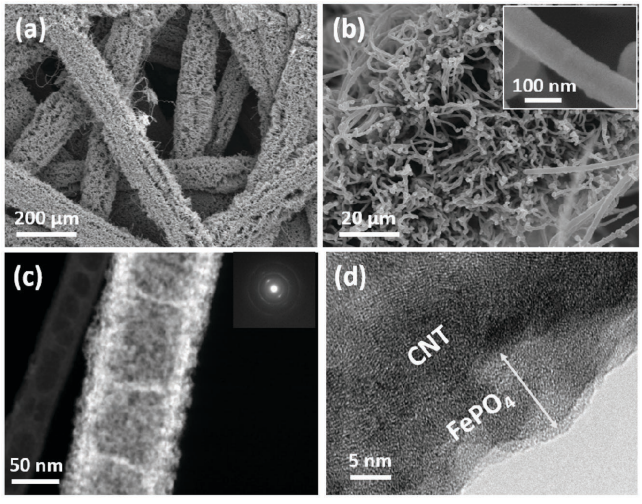

Figure 1. a,b) SEM images of 400-cycle CNTs@$FePO_4$ on carbon papers; c) STEM and d) HRTEM images of 400-cycle CNTs@$FePO_4$ (insert in panel (c) shows its corresponding SAD pattern).

The morphology and structure of the 400-cycle CNTs@$FePO_4$ on carbon papers are shown in **Figure 1**. The carbon papers are composed of crossover carbon fibers, and remain porous structure after the growth of aligned CNTs on them, as seen in Figure 1a. These open spaces allow the efficient diffusion of gaseous ALD precursors to the surface of CNTs, therefore maximizing the coverage of active materials ($FePO_4$ and Li_3PO_4) deposited on the 3D CNTs structures. After the first step as shown in Scheme 1, the tubular CNTs are covered with a uniform layer of $FePO_4$ (Figure 1b), which can be clearly observed as a bright coating on the outer surface of CNTs in the scanning transmission electron microscopy (STEM) image (Figure 1c). Further analysis by selected area diffraction (SAD) pattern and high-resolution transmission electron microscope (HRTEM) discloses the disordered nature of the as-deposited $FePO_4$, as seen in Figure 1c,d. The Fe/P ratio of the amorphous $FePO_4$ is determined to be ≈1.2 by energy dispersive spectroscopy (EDS) analysis (Figure S1, Supporting Information). The $FePO_4$ layer deposited by using 400 ALD cycles is around 12 nm in thickness, as shown in Figure 1d. The result in Figure 1 confirms the successful deposition of amorphous $FePO_4$ in the 3D CNTs structure by ALD.

The electrochemical performance of 200-cycle and 400-cycle CNTs@$FePO_4$ was evaluated in LIBs and SIBs, and the results are shown in **Figure 2**. Figure 2a,b presents the cyclic voltammetry (CV) curves of 400-cycle CNTs@$FePO_4$ measured between 1.5 and 4.0 V at scanning rates from 1 to 100 mV s^{-1} for LIBs and SIBs, respectively. The 400-cycle CNTs@$FePO_4$ shows broad reduction and oxidation peaks in both LIBs and SIBs, which are typically observed in amorphous $FePO_4$.[25,27,28] At a scanning rate of 50 mV s^{-1}, the reduction and oxidation peaks of 400-cycle CNTs@$FePO_4$ locate at about 2.0 and 3.2 V, respectively. With the increase of the scanning rate from 1 to 100 mV s^{-1}, the redox peaks remain in the presented voltage range, indicating the excellent electronic conductivity and ionic diffusion in 3D CNTs@$FePO_4$ structure. In addition, the

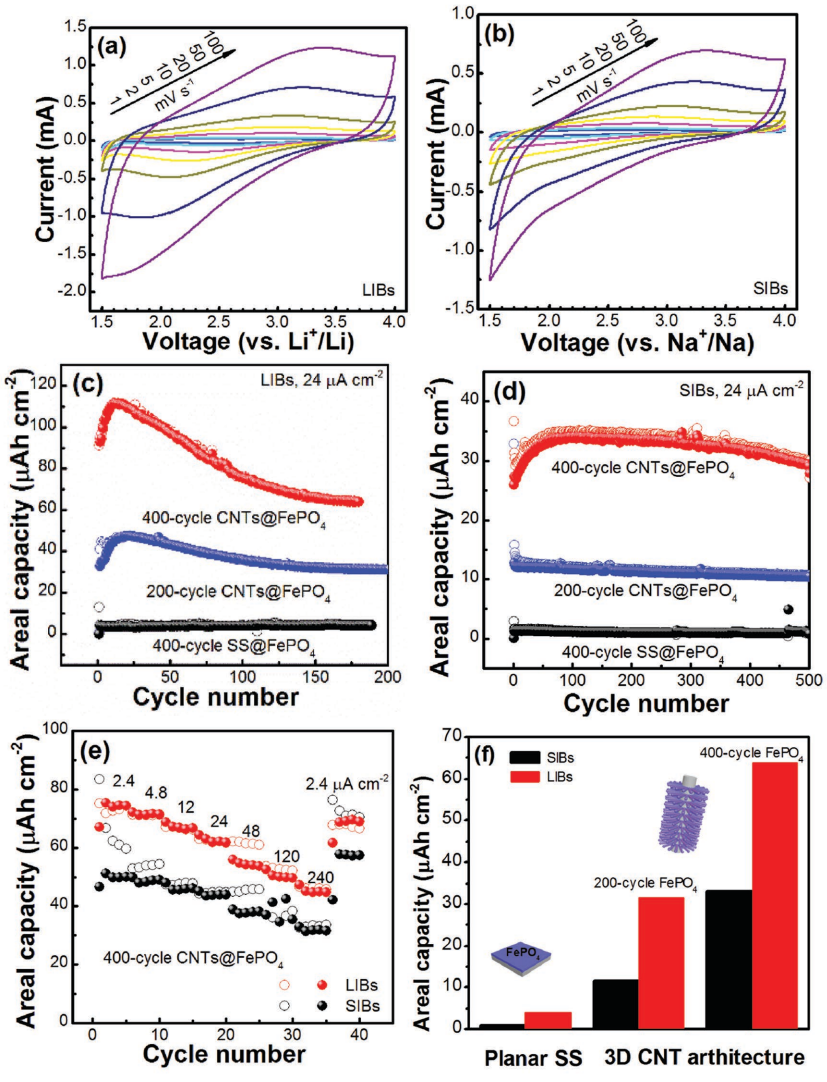

Figure 2. CV curves of 400-cycle CNTs@$FePO_4$ for a) LIBs and b) SIBs; cycling performance of 400-cycle CNTs@$FePO_4$ (red), 200-cycle CNTs@$FePO_4$ (blue), and 400-cycle SS@$FePO_4$ (black) at 24 μA cm^{-2} for c) LIBs and d) SIBs; e) rate capability of 400-cycle CNTs@$FePO_4$ at different current densities from 2.4 to 240 μA cm^{-2}; and f) comparison of LIB and SIB areal capacities at the 180th cycle for $FePO_4$ on planar SS and 3D CNT architecture.

oxidation/reduction potentials of amorphous $FePO_4$ in LIBs are ≈0.2–0.3V higher than these in SIBs (as seen in Figure S2, Supporting Information) due to the lower standard electrochemical potential of Li metal (–3.0V vs S.H.E.) than that of Na metal (–2.7V vs S.H.E.).[21,22] The cycling stabilities of 200-cycle and 400-cycle CNTs@$FePO_4$ are examined at a current density of 24 μA cm^{-2}, and compared to that of 400-cycle SS@$FePO_4$. It can be seen in Figure 2c,d that 3D CNTs@$FePO_4$ structure exhibits significantly higher areal capacities than 2D SS@$FePO_4$ in LIBs and SIBs. For LIBs, 400-cycle SS@$FePO_4$ can only deliver an areal capacity of about 4 μAh cm^{-2} (Figure 2c). In the sharp contrast, 200-cycle and 400-cycle CNTs@$FePO_4$ exhibit initial discharge capacities of 32 and 92 μAh cm^{-2}, i.e., 8 times and 23 times that of the SS@$FePO_4$ electrode, respectively. Both 200-cycle and 400-cycle CNTs@$FePO_4$ experience a capacity increase in the first ten cycles, and then gradual capacity decay afterward. Charge–discharge profile of 200-CNTs@$FePO_4$ becomes less polarized after the first two cycles (Figure S3a, Supporting Information). The phenomena of capacity increase and less polarization in the initial stage might be due to the structure reordering of the amorphous $FePO_4$ during lithium insertion and extraction processes. The polarization of charge–discharge curves gradually becomes larger after the first ten cycles (Figure S3, Supporting Information), resulting in the capacity decay as observed in Figure 2c. The reasons for the increased polarization and capacity decay will be discussed later on. After 180 battery cycles, the 200-cycle and 400-cycle CNTs@$FePO_4$ maintain areal capacities of 31 and 65 μAh cm^{-2}, which are still ≈5 times and 11 times higher than that of 400-cycle $FePO_4$@SS, respectively. Moreover, both 200-cycle and 400-cycle CNTs@$FePO_4$ exhibit higher Coulombic efficiency than 400-cycle $FePO_4$@SS, as shown in Figure S4a (Supporting Information). The pristine CNTs on carbon papers without $FePO_4$ coating contribute an areal capacity of ≈9 μAh cm^{-2} to the overall capacity of CNTs@$FePO_4$ in LIBs (Figure S5, Supporting Information). As tested in SIBs, 200-cycle and 400-cycle CNTs@$FePO_4$ exhibit areal capacities of 13 and 25 μAh cm^{-2}, respectively in the first cycle, whereas only 2 μAh cm^{-2} discharge capacity can be extracted in 400-cycle SS@$FePO_4$ (Figure 2d). Additionally, 3D CNTs@$FePO_4$ structure shows a very stable cycling performance and high Coulombic efficiency in SIBs (Figure S4b, Supporting Information). After 500 battery cycles, 200-cycle and 400-cycle CNTs@$FePO_4$ can maintain areal capacities of 11 and 30 μAh cm^{-2}, respectively. The pristine CNTs on carbon papers deliver an areal capacity of ≈4 μAh cm^{-2} in SIBs (Figure S5, Supporting Information). Apparently, the 3D CNTs@$FePO_4$ delivers relatively lower areal capacities in SIBs than LIBs. The reasons can be attributed to the sluggish kinetics of Na^+ in the amorphous $FePO_4$ compared to Li^+, and the higher electrochemical potential of Na metal than Li metal.[23,29] The rate performance of 3D CNTs@$FePO_4$ are evaluated at current densities from 2.4 to 240 μA cm^{-2}, and the result is shown in Figure 2e. It can be seen that 400-cycle CNTs@$FePO_4$ can deliver lithium storage capacities of 75, 72, 68, 63, 55, 51, and 47 μAh cm^{-2}, and sodium storage capacities of 52, 49, 47, 45, 38, 35, and 33 μAh cm^{-2}, at current densities of 2.4, 4.8, 12, 24, 48, 120, and 240 μA cm^{-2}, respectively. The discharge capacities for both LIBs and SIBs can be restored, when the current density changes from 240 to 2.4 μA cm^{-2}. Figure 2e clearly indicates the extraordinary rate capability of 3D CNTs@$FePO_4$, which can be attributed to the unique 3D CNTs@$FePO_4$ structure on carbon papers. The open structure of 3D CNTs

structure maximize the contact area between $FePO_4$ and electrolytes, and the thin $FePO_4$ layer on CNTs enabled by ALD provides short diffusion paths for Li^+/Na^+. The areal capacities of $FePO_4$ on 2D SS and 3D CNT substrates after 180 cycles are compared in Figure 2f. The areal capacities of 400-cycle CNTs@$FePO_4$ are 16 and 33 times higher than those of 400-cycle SS@$FePO_4$ electrode for LIBs and SIBs, respectively. Furthermore, the areal capacity of 3D CNTs@$FePO_4$ can be easily controlled by using different ALD cycles of $FePO_4$, because the thickness of $FePO_4$ is linearly dependent on ALD cycles.[25] For example, the 400-cycle CNTs@$FePO_4$ exhibits doubled areal capacity than the 200-cycle CNTs@$FePO_4$ in LIBs and SIBs, as shown in Figure 2f. The areal capacity of 3D CNTs@$FePO_4$ could be further increased by repeating ALD cycles until amorphous $FePO_4$ with a desirable thickness is reached. The results in Figure 2 indicates that ALD is an effective approach to fabricate 3D CNTs@$FePO_4$ architecture with high areal capacity and excellent rate capability for Li^+ and Na^+ storage.

Integration of solid-state electrolytes onto 3D electrode structure is an essential step in order to build 3D microbatteries, but remains a big challenge due to the complexity of the system. Interface stability between the electrode and electrolyte is critical to 3D microbatteries, and the interfacial side reactions could be detrimental to the performance of microbatteries.[30,31] In this work, to demonstrate the ability of ALD to construct complicated 3D structured microbatteries, the 400-cycle CNTs@$FePO_4$ is further coated with solid-state electrolyte Li_3PO_4 by using 200 ALD cycles (Scheme 1). From **Figure 3**a, there is no obvious difference observed between CNTs@$FePO_4$@Li_3PO_4 and CNTs@$FePO_4$ (Figure 1b). The coating thickness on the surface of CNTs is measured to be 20 nm from the HRTEM image (Figure 3b), which clearly shows distinguished region assignable to CNT core and $FePO_4$@Li_3PO_4 outer layer. Li_3PO_4 and $FePO_4$ cannot be differentiated from microscopic characterizations, because of the amorphous nature of both thin films. Nevertheless, EDS analysis discloses that the Fe/P ratio for CNTs@$FePO_4$@Li_3PO_4 (≈0.8) is lower than that of CNTs@$FePO_4$ (≈1.2) (Figure S1, Supporting Information), suggesting the successful coating of Li_3PO_4. The thickness of Li_3PO_4 is calculated to be ≈8 nm by subtracting the thickness of $FePO_4$ from the total thickness of $FePO_4$@Li_3PO_4 (Figure 1c).

Electrochemical stability of CNTs@$FePO_4$@Li_3PO_4 for LIBs is evaluated with liquid ethylene carbonate (EC):diethyl carbonate (DEC):ethyl methyl carbonate (EMC) electrolyte, and compared to that of CNTs@$FePO_4$ (Figure 3c). The CNTs@$FePO_4$@Li_3PO_4 can deliver an areal capacity of 35 μAh cm^{-2} in the first cycle, which is about one third of the initial capacity of CNTs@$FePO_4$. The main reason for the lower capacity of CNTs@$FePO_4$@Li_3PO_4 is due to the reduced ionic conductivity of Li_3PO_4 solid-state electrolyte (≈10^{-9} S cm^{-1} at RT) compared to that of liquid ones (generally ≈10^{-3} S cm^{-1} at RT),[13] which slows down the Li^+ diffusion into/out of $FePO_4$ active material. Therefore, solid-state electrolytes with a higher ionic conductivity should be pursued for surface coating purpose in future. Nevertheless, the CNTs@$FePO_4$@Li_3PO_4 structure is proven to be electrochemically active for lithium-ion storage. CV testing on CNTs@$FePO_4$@Li_3PO_4 detects clear reduction and oxidation peaks at 2.7/3.5 V respectively, which is higher than 2.5/3.3 V for CNTs@$FePO_4$ (Figure 3d). One possible explanation for the voltage shift is compositional/structural changes of $FePO_4$ during Li_3PO_4 solid-state electrolyte coating. During the ALD deposition process, Li ions in the Li_3PO_4 coating layer might diffuse into $FePO_4$ active materials, partial of which might transform to amorphous $LiFePO_4$ with higher redox potentials. Similar Li ions diffusion into active materials during ALD deposition process has been observed in a previous work.[18] This result implies that the solid-state electrolyte coating might affect the electrochemical intercalation/deintercalation mechanism in the $FePO_4$ electrode. From Figure 3c, it can also be found that the cycling performance of CNTs@$FePO_4$@Li_3PO_4 is much more stable than that of CNTs@$FePO_4$. The areal capacity of CNTs@$FePO_4$@Li_3PO_4 even increases from 35 to 40 μAh cm^{-2} after 150 cycles, whereas the capacity of CNTs@$FePO_4$ drops from 92 to 66 μAh cm^{-2} in the same condition. This result suggests that the Li_3PO_4 coating can stabilize the interface between $FePO_4$ and liquid electrolytes.

In order to find out the underlying mechanism for the improved electrochemical stability of $FePO_4$ electrodes by solid-state electrolyte coating, Hard X-ray photoemission spectroscopy (HXPES) was employed to investigate the solid-electrolyte interphase (SEI) on SS@$FePO_4$@$Li_3PO_4$and SS@$FePO_4$ (as schematically shown in **Figure 4**). HXPES

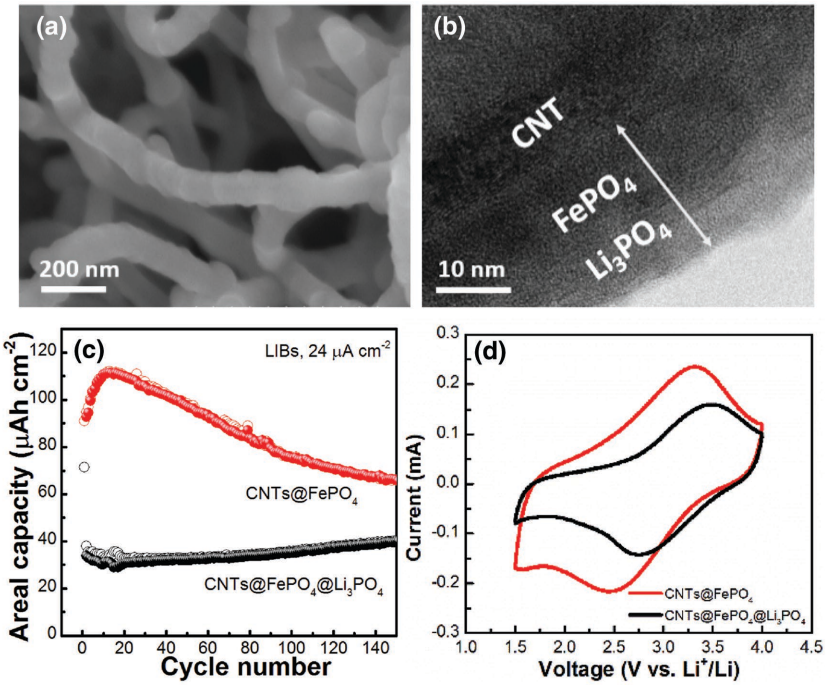

Figure 3. a) SEM image and b) HRTEM image of CNTs@$FePO_4$@Li_3PO_4; c) cycling stability and d) CV curves of CNTs@$FePO_4$@Li_3PO_4 (black) and CNTs@$FePO_4$ (red) at 5 mV s^{-1} after 150 cycles.

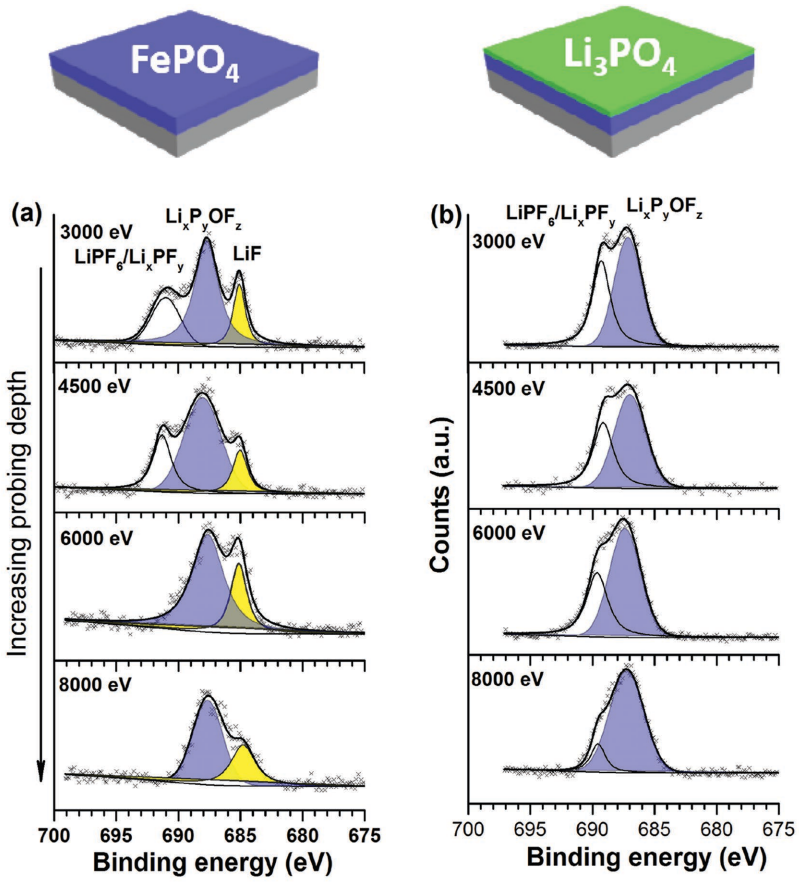

Figure 4. HXPES F1s spectra for a) SS@$FePO_4$ and b) SS@$FePO_4$@Li_3PO_4. The photon energy was tuned from 3 to 8 keV in order to change the detection depth.[26]

is able to provide chemical information in depth not limited to the surface but extended beyond 10 nm in bulk samples, compared to laboratory XPS. The depth profile of a certain element can be achieved by tuning the excitation photon energy and thus changing the kinetic energy of the photon energy from the core level of interest; this in turn changes the probing depth as described by the universal curve where the escape depth λ (1/e attenuation length) depends linearly on the square root of the kinetic energy of the photon electron beyond the minimum.[32,33] For example, the F 1s photoelectron (BE ≈685 eV) will have kinetic energy of 2310 eV (3000–685–5 (work function)) at 3000 eV photon energy with a corresponding λ of ≈3.5 nm while with 8000 eV photons, λ increases to ≈6 nm depth. Therefore, HXPES is a powerful tool for non-destructive depth-resolved analysis on the compositions of SEI layers.[26,34,35] The SS@$FePO_4$ and SS@$FePO_4$@Li_3PO_4 for HXPES measurements were harvested from coil-type half cells pre-cycled for 150 cycles in LIBs, and washed with the DEC solution. The F1s spectra for both samples are collected at excitation energies of 3.0, 4.5, 6.0, and 8 keV with increasing probing depth, and the results are illustrated in Figure 4. The F1s spectrum of SS@$FePO_4$ show two dominant peaks at 685.0 and 688.1 eV (Figure 4a) at all the probing depths, which are characteristic of LiF and $Li_xP_yOF_z$, respectively.[36–38] In addition, another peak at 691.3 eV is found in the shallow surface of SS@$FePO_4$ using photon energies of 3.0 and 4.5 keV, and can be assigned to $LiPF_6$ and/or Li_xPF_y.[37] This is probably due to residual $LiPF_6$ salt on the surface of SS@$FePO_4$. For SS@$FePO_4$@Li_3PO_4, the F1s spectrum can be fitted into two peaks at about 688.1 and 690.0 eV, which are ascribed to $Li_xP_yOF_z$ and $LiPF_6$/Li_xPF_y respectively.[36–38] The reduced intensity of 690.0 eV peak with higher photon energies is consistent with the trend observed in the same peak in Figure 4a, suggesting that this peak is mainly contributed from $LiPF_6$ salt remaining on the sample surface. Compared Figure 4a,b, it can be found that $Li_xP_yOF_z$ is the dominant component in the F1s spectra of both SS@$FePO_4$@Li_3PO_4 and SS@$FePO_4$, while LiF is only present in SS@$FePO_4$. The HXPES result shows that the Li_3PO_4 coating on $FePO_4$ prevents the formation of LiF in the SEI layer, which is believed to be one of the main reasons for the performance degradation in CNTs@$FePO_4$ (Figure 3c). Previous studies have shown that precipitation of LiF could lead to an insulating SEI layer on the electrodes, which was detrimental to the cycling performance of the cathode.[39,40] The formation of LiF stemmed from a series of side reactions at the electrode/electrolyte interface. One is from thermal decomposition of $LiPF_6$ in the electrolyte, in particular at high temperatures ($LiPF_6 \rightarrow LiF + PF_5$).[39,41] The PF_5 by-product is highly reactive with traceable amounts of water in the electrolyte to form HF ($PF_5 + H_2O \rightarrow POF_3 + 2HF$).[39,41] The produced HF can react with the oxide in the cathode to form LiF and H_2O.[36,42] The generated H_2O triggers further side reactions to produce more LiF, which would precipitate in the SEI layer on $FePO_4$ and build up charger transfer resistance. In SS@$FePO_4$@Li_3PO_4, the Li_3PO_4 coating prevents the direct contact between $FePO_4$ and liquid electrolytes, thus greatly alleviating the side reactions that lead to the formation of LiF. Another possible reason for decreasing capacity in CNTs@$FePO_4$ is the dissolution of irons into the electrolyte by the etching of HF generated in the above side reactions.[43] In fact, ultrathin surface coatings by ALD have been widely used on the cathode materials to improve their cycling performance and rate capability in LIBs, especially at extreme cycling conditions (such as high temperature, high voltage).[6–9] The reason for performance improvement was generally attributed to the alleviated metal dissolutions from the cathode materials by ALD surface coatings.[9,44] The present result suggests that the formation of undesirable LiF in the SEI layer is another contributor to the decreased performance in the cathode, in addition to metal dissolutions by HF. Another recent work by Lin and co-workers showed that ALD-LiPON coating enhanced the cyclability of CNTs@RuO_2 conversion electrodes, due to the high Li ion conductivity at the electrode/electrolyte interface and constrained RuO_2 electrodes

by LiPON coating.[45] Both work on LiPON and Li_3PO_4 coatings indicate that the solid-state electrolyte is critical for transporting Li ions through the electrode/electrolyte interface, regardless of on the anode or cathode. Differently, this work reveals that solid-state electrolyte coating not only constrains the electrode materials mechanically, but also affects the formation and composition of SEI layers by acting as a side-reaction barrier. The influence of surface coatings by ALD on the SEI layers of the cathode and anode should be considered and deserves more detailed studies in future. Another implication of this work is that solid-state electrolyte by ALD can be employed as an ion-conductive coating on the cathode materials of LIBs to improve their cycling stability. In this regard, solid-state electrolytes with high ionic conductivity (>10^{-6} S cm^{-1}) should be pursued in future. This work suggests that solid-state electrolyte coating by ALD can be adopted for 3D electrodes in LIBs with liquid electrolytes to achieve better cycling stabilities. Future work will be focused on the integration of ALD anode onto the present 3D substrate/cathode/electrolyte system with the aim of fabricating a full 3D all-solid-state microbatteries.

3. Conclusion

In summary, we successfully applied ALD technique to fabricate 3D CNTs@$FePO_4$ architecture as a 3D electrode for LIBs and SIBs. The 3D structured CNTs@$FePO_4$ exhibited much higher areal capacities than $FePO_4$ deposited on a planar SS substrate in both LIBs and SIBs. The areal capacity of CNTs@$FePO_4$ was proportional to the thickness of $FePO_4$ active material on CNTs, which was easily controlled by tuning ALD cycle number. Moreover, Li_3PO_4 solid-state electrolyte was incorporated onto the 3D CNTs@$FePO_4$, and the hybrid 3D CNTs@$FePO_4$@Li_3PO_4 structure showed improved cycling stabilities in LIBs. Furthermore, Li_3PO_4 solid-state electrolyte improved the stability of CNTs@$FePO_4$ as a surface coating, by preventing the formation of LiF in the SEI layer. HXPES as a powerful depth profiling tool for SEI studies in batteries was demonstrated. This ALD approach presented in this work can be extended to fabricate a variety of electrode materials for battery applications.

4. Experimental Section

ALD Fabrication of 3D $FePO_4$ Electrodes: Nitrogen-doped CNTs on carbon papers were chosen as the 3D substrate for $FePO_4$. The CNTs on CP were synthesized by using a CVD method as described previously.[24] These CNTs on carbon papers were loaded in a Savannah 100 ALD system (Ultratech/Cambridge Nanotech., USA) for the deposition of $FePO_4$ and Li_3PO_4 materials. The ALD of $FePO_4$ on CNTs was carried out at 300 °C, by using ferrocene, ozone, trimethylphosphate, and water as precursors,[25] and the prepared sample was designated as CNTs@$FePO_4$ hereafter. Li_3PO_4 was coated on CNTs@$FePO_4$ at 250 °C by ALD, using lithium tert-butoxide and trimethylphosphate as precursors,[13] and the obtained sample was defined as CNTs@$FePO_4$@Li_3PO_4. SS foils were used as a 2D substrate in comparison with 3D CNTs substrates. The same ALD processes were performed on SS foils as above. The SS foils were cleaned with acetone and alcohol three times before being loading into the ALD chamber. The obtained samples were designated as SS@$FePO_4$ and SS@$FePO_4$@Li_3PO_4.

Physical Characterizations: The morphology and structure of the above samples were characterized by using field-emission SEM (Hitachi S-4800) and HRTEM (JEOL 2010 FEG) equipped with EDS. HXPES measurement at F1s was performed on cycled SS@$FePO_4$ and SS@$FePO_4$@Li_3PO_4, at Soft X-ray Microcharacterization Beamline (SXRMB) at the Canadian Light Source (CLS) located at the University of Saskatoon, Saskatoon, Canada. The detection depth of HXPES was able to be adjusted by tuning the photon energy from 3 to 8 keV.[26]

Electrochemical Characterizations: The electrochemical performance of $FePO_4$ and $FePO_4$@Li_3PO_4 on both 2D and 3D substrates was tested in coin-type half cells, using an Li or Na metal foils as the counter electrode for LIBs and SIBs, respectively. The electrolyte for LIBs was 1 M $LiPF_6$ in the solution of EC, DEC, and EMC with a volume ratio of 1:1:1, and Celgard 2400 was used as the separator. The electrolyte for SIBs was 1 M $NaClO_4$ in the solution of EC and propylene carbonate with a volume ratio of 1:1, and Celgard 3501 was used as the separator. The coin-type half cells were assembled in an argon-filled glove box with O_2 and H_2O level below 1 ppm. Charge–discharge cycling at a constant current mode was performed on Arbin BT-2000 Battery Test System, and CV was tested on the versatile multichannel potentiostat 3/Z (VMP3). All electrochemical measurements were carried out in a voltage range of 1.5–4.0 V at RT.

Supporting Information

Supporting Information is available from the Wiley Online Library or from the author.

Acknowledgements

This work was supported by Nature Sciences and Engineering Research Council of Canada (NSERC), Canada Research Chair (CRC) Program, Canada Foundation for Innovation (CFI), Ontario Research Fund (ORF), the Canadian Light Source (CLS), the Canadian Centre for Electron Microscopy (CCEM) at McMaster University, and the University of Western Ontario. The CLS is supported by CFI, NSERC, NRC, CHIR, and the University of Saskatchewan. Q.S. and B.W. acknowledge the receipt of support from the CLS Post-Doctoral Student Travel Support Program. The authors really appreciate the technical support from Dr. Qunfeng Xiao and Dr. Yongfeng Hu at the SXRMB Beamline at CLS. J.L. is grateful to the NSERC Postdoctoral Fellowship (PDF) Program.

Received: May 23, 2016
Revised: July 3, 2016
Published online:

[1] M. Roberts, P. Johns, J. Owen, D. Brandell, K. Edstrom, G. E. Enany, C. Guery, D. Golodnitsky, M. Lacey, C. Lecoeur, H. Mazor, E. Peled, E. Perre, M. M. Shaijumon, P. Simon, P.-L. Taberna, *J. Mater. Chem.* **2011**, *21*, 9876.
[2] J. F. M. Oudenhoven, L. Baggetto, P. H. L. Notten, *Adv. Energy Mater.* **2011**, *1*, 10.
[3] J. W. Elam, D. Routkevitch, P. P. Mardilovich, S. M. George, *Chem. Mater.* **2003**, *15*, 3507.
[4] S. M. George, *Chem. Rev.* **2010**, *110*, 111.
[5] V. Miikkulainen, M. Leskelä, M. Ritala, R. L. Puurunen, *J. Appl. Phys.* **2013**, *113*, 021301.
[6] X. Meng, X.-Q. Yang, X. Sun, *Adv. Mater.* **2012**, *24*, 3589.
[7] H. C. M. Knoops, M. E. Donders, M. C. M. van de Sanden, P. H. L. Notten, W. M. M. Kessels, *J. Vac. Sci. Technol., A* **2012**, *30*, 010801.

[8] O. Nilsen, V. Mikkulainen, K. B. Gandrud, E. Østreng, A. Ruud, H. Fjellvåg, *Phys. Status Solidi A* **2014**, *211*, 357.
[9] J. Liu, X. Sun, *Nanotechnology* **2015**, *26*, 024001.
[10] X. Meng, J. A. Libera, T. T. Fister, H. Zhou, J. K. Hedlund, P. Fenter, J. W. Elam, *Chem. Mater.* **2014**, *26*, 1029.
[11] J. Liu, M. N. Banis, X. Li, A. Lushington, M. Cai, R. Li, T.-K. Sham, X. Sun, *J. Phys. Chem. C* **2013**, *117*, 20260.
[12] J. Hamalainen, J. Holopainen, F. Munnik, T. Hatanpaa, M. Heikkila, M. Ritala, M. Leskela, *J. Electrochem. Soc.* **2012**, *159*, A259.
[13] B. Wang, J. Liu, Q. Sun, R. Li, T.-K. Sham, X. Sun, *Nanotechnology* **2014**, *25*, 504007.
[14] Y. C. Perng, J. Cho, S. Y. Sun, D. Membreno, N. Cirigliano, B. Dunn, J. P. Chang, *J. Mater. Chem. A* **2014**, *2*, 9566.
[15] A. C. Kozen, A. J. Pearse, C. F. Lin, M. Noked, G. W. Rubloff, *Chem. Mater.* **2015**, *27*, 5324.
[16] M. Nisula, Y. Shindo, H. Koga, M. Karppinen, *Chem. Mater.* **2015**, *27*, 6987.
[17] M. E. Donders, W. M. Arnoldbik, H. C. M. Knoops, W. M. M. Kessels, P. H. L. Notten, *J. Electrochem. Soc.* **2013**, *160*, A3066.
[18] V. Miikkulainen, A. Ruud, E. Østreng, O. Nilsen, M. Laitinen, T. Sajavaara, H. Fjellvåg, *J. Phys. Chem. C* **2014**, *118*, 1258.
[19] J. Liu, M. N. Banis, Q. Sun, A. Lushington, R. Li, T.-K. Sham, X. Sun, *Adv. Mater.* **2014**, *26*, 6472.
[20] M. Nisula, M. Parppinen, *Nano Lett.* **2016**, *16*, 1276.
[21] N. Yabuuchi, K. Kubota, M. Dahbi, S. Komaba, *Chem. Rev.* **2014**, *114*, 11636.
[22] M. D. Slater, D. Kim, E. Kee, C. S. Johnson, *Adv. Funct. Mater.* **2013**, *23*, 947.
[23] J. Liu, M. N. Banis, B. Xiao, Q. Sun, A. Lushington, R. Li, J. Guo, T. K. Sham, X. Sun, *J. Mater. Chem. A* **2015**, *3*, 24281.
[24] Y. Zhong, M. Jaidann, Y. Zhang, G. Zhang, H. Liu, M. I. Ionescu, R. Li, X. Sun, H. Abou-Rachid, L. S. Lussier, *J. Phys. Chem. Solid* **2010**, *71*, 134.
[25] J. Liu, B. Xiao, M. N. Banis, R. Li, T.-K. Sham, X. Sun, *Electrochem. Acta* **2014**, *162*, 275.
[26] Q. Xiao, X. Cui, Y. Shi, Y. Hu, T. K. Sham, H. Piao, J. Mcmahon, *Can. J. Chem.* **2015**, *93*, 113.
[27] T. Liu, Y. Duan, G. Zhang, M. Li, Y. Feng, J. Hu, J. Zheng, J. Chen, F. Pan, *J. Mater. Chem. A* **2016**, *4*, 4479.
[28] Y. Fang, L. Xiao, J. Qiao, X. Ai, H. Yag, Y. Cao, *Nano Lett.* **2014**, *14*, 3539.
[29] Q. Fan, L. Lei, G. Yin, Y. Chen, Y. Sun, *Electrochem. Commun.* **2014**, *38*, 120.
[30] W. D. Richards, L. J. Miara, Y. Wang, J. C. Kim, G. Ceder, *Chem. Mater.* **2016**, *28*, 266.
[31] J. H. Woo, J. E. Trevey, A. S. Cavanagh, Y. S. Choi, S. C. Kim, S. M. George, K. H. Oh, S. H. Lee, *J. Electrochem. Soc.* **2012**, *159*, A1120.
[32] K. Kobayashi, M. Yabashi, Y. Takata, T. Tokushima, S. Shin, K. Tamasaku, D. Miwa, T. Ishikawa, H. Nohira, T. Hattori, Y. Sugita, O. Najatsuka, A. Sakai, S. Zaima, *Appl. Phys. Lett.* **2003**, *83*, 1005.
[33] S. Thiess, C. Kunz, B. C. C. Cowie, T.-L. Lee, M. Renier, J. Zegenhagen, *Solid State Commun.* **2004**, *132*, 589.
[34] B. Philippe, R. Dedryvère, M. Gorgoi, H. Rensmo, D. Gonbeau, K. Edström, *J. Am. Chem. Soc.* **2013**, *135*, 9829.
[35] B. Philippe, M. Hahlin, K. Edström, T. Gustafsson, H. Siegbahn, H. Rensmo, *J. Electrochem. Soc.* **2016**, *163*, A178.
[36] A. M. Andersson, D. P. Abraham, R. Haasch, S. MacLaren, J. Liu, K. Amine, *J. Electrochem. Soc.* **2002**, *149*, A1358.
[37] M. Nie, J. Demeaux, B. T. Young, D. R. Heskett, Y. Chen, A. Bose, J. C. Woicik, B. L. Lucht, *J. Electrochem. Soc.* **2015**, *162*, A7008.
[38] W. Li, B. L. Lucht, *J. Electrochem. Soc.* **2006**, *153*, A1617.
[39] M. Balasubramanian, H. S. Lee, X. Sun, X. Q. Yang, A. R. Moodenbaugh, J. Mcbreen, D. A. Fischer, Z. Fu, *Electrochem. Solid-State Lett.* **2002**, *5*, A22.
[40] K. Y. Chung, W. S. Yoon, K. B. Kim, B. W. Cho, X. Q. Yang, *J. Appl. Electrochem.* **2011**, *41*, 1295.
[41] S. E. Sloop, J. K. Pugh, S. Wang, J. B. Kerr, K. Kinoshita, *Electrochem. Solid-State Lett.* **2001**, *4*, A42.
[42] J. L. Tebbe, A. M. Holder, C. B. Musgrave, *ACS Appl. Mater. Interfaces* **2015**, *7*, 24265.
[43] J. Wang, J. Yang, Y. Zhang, Y. Li, Y. Tang, M. N. Banis, X. Li, G. Liang, R. Li, X. Sun, *Adv. Funct. Mater.* **2013**, *23*, 806.
[44] X. Li, J. Liu, X. Meng, Y. Tang, M. N. Banis, J. Yang, Y. Hu, R. Li, M. Cai, X. Sun, *J. Power Sources* **2014**, *247*, 57.
[45] C. F. Lin, M. Noked, A. C. Kozen, C. Liu, O. Zhao, K. Gregorczyk, L. Hu, S. B. Lee, G. W. Rubloff, *ACS Nano* **2016**, *10*, 2693.